



pubs.acs.org/acsapm Article

# Flexible Polymer-Based Nanodielectrics Reinforced with Electrospun Composite Nanofibers for Capacitive Energy Storage

Stavros X. Drakopoulos,\* Jing Yang, Orestis Vryonis, Leah Williams, Georgios C. Psarras, and Elisa Mele



Cite This: ACS Appl. Polym. Mater. 2022, 4, 8203-8215



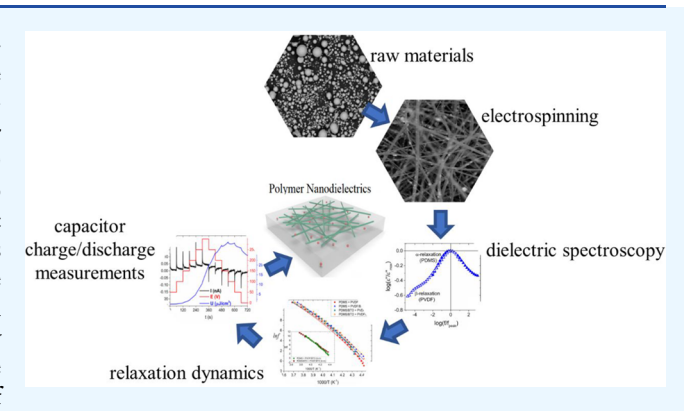
**ACCESS** 

III Metrics & More

Article Recommendations

Supporting Information

ABSTRACT: Nanocomposite materials based on polydimethylsiloxane (PDMS) reinforced by electrospun poly(vinylidene fluoride) (PVDF) nanofibers and barium titanate (BTO) nanoparticles were fabricated and tested as dielectric materials for capacitive energy storage applications. Two types of BTO nanoparticles were examined, prior and after ball milling, to investigate the effect of interfacial area and size on the dielectric properties. The morphology of the produced PVDF nanofibers was evaluated via scanning electron microscopy (SEM) to ensure the optimum electrospinning conditions and verify the incorporation of BTO nanoparticles. The composite systems were analyzed by dielectric spectroscopy, and three dielectric processes were revealed: the dynamic glass-to-rubber transition processes of



PDMS and PVDF and an interfacial polarization process. It was observed that the dynamic glass-to-rubber transition process of the PVDF nanofibers strongly depends on the size of the BTO nanoparticles that introduce confinement effects and affect thus the temperature dependence of the relaxation. In addition, as verified by ac conductivity, ball milling reduced the conduction of the nanocomposites by 80%, indicating the increase of the charge carrier trapping area around the BTO nanoparticles. Finally, the developed nanocomposites were tested as dielectric materials for capacitor applications at room temperature conducting charge/discharge measurements under the influence of a dc electric field, and their discharge performance and efficiency were examined at various dc voltages (50–300 V) and cycle life. Here, experimental evidence regarding the importance of interfacial area on the energy storage performance in nanodielectrics is presented that will aid the development of more efficient energy materials.

KEYWORDS: nanodielectrics, electrospinning, PDMS, energy storage, nanocomposites

#### 1. INTRODUCTION

With the increasing demand of energy toward the development of global economy, energy storage and harvesting are important areas for science, engineering, and society. Considering the depletion of fossil fuels and the urgency caused by climate change, renewable energy sources need to be utilized and efficient electrical storage devices need to be developed.<sup>2,3</sup> To meet both environmental and socioeconomic requirements, new energy materials characterized by high efficiency, low cost, and eco-friendly properties are required. Among the three major types of electrical storage devices (dielectric capacitors, supercapacitors, and batteries) dielectrics are promising candidates as renewable electrical storage devices due to their long lifetime and cycling stability. However, they suffer from low energy density values, an issue that has attracted significant research interest over the past decades and led to the development of "nanodielectrics".4,5

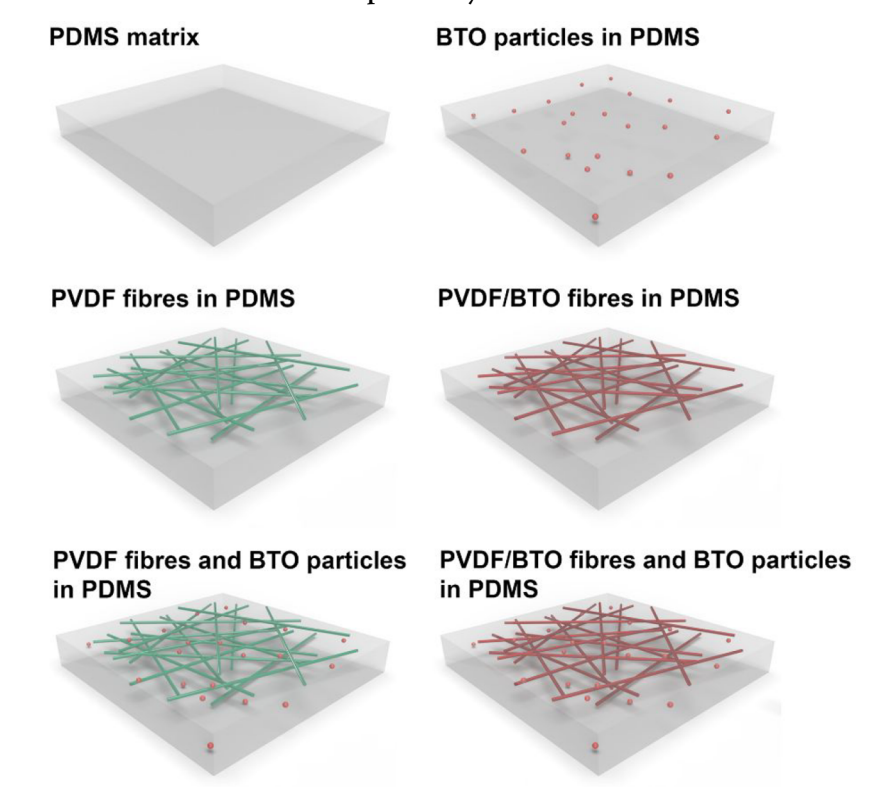
Despite their significantly low dielectric permittivity, polymers are an attractive choice for lightweight electrical energy storage applications due to their insulating properties that result in high breakdown strength values. 6–8 To enhance the dielectric permittivity without compromising the breakdown strength, high-permittivity insulating/semiconducting nanofillers are employed, introducing thus the aforementioned new class of materials, namely polymer nanodielectrics. 9–11 The current benchmark of capacitor applications is pristine biaxially oriented polypropylene which exhibits high breakdown strength, ultralow dielectric loss, and easy processability but suffers from low dielectric constant and low volumetric energy density. Poly(vinylidene fluoride) (PVDF) has been one of the most studied polymers for its dielectric and piezoelectric properties, and it is considered one of the best candidates for capacitive energy storage in capacitor

Received: July 5, 2022 Accepted: October 9, 2022 Published: October 18, 2022





Scheme 1. Schematic Illustration of the Different Samples Analyzed<sup>a</sup>



<sup>a</sup>The PDMS matrix is represented as a gray slab; the BTO particles are represented as red spheres; the PVDF electrospun fibers are represented as green cylinders; the PVDF electrospun fibers embedding BTO nanoparticles (PVDF/BTO) are depicted as red cylinders.

applications, especially when combined to BTO nanoparticles. 13,14

In nanodielectric systems, the interfacial characteristics govern the resulting dielectric properties and thus the energy storage and harvesting performance. 15,16 A way to increase and control the interfacial area between the constituents of a nanodielectric system and thus their interfacial interactions in energy materials is by employing fiber fabrication techniques like electrospinning.  $^{17,18}$  The multifunctional character of electrospun fibers is based on their high surface area and porosity that make them particularly interesting for energy storage applications, such as batteries, supercapacitors, and dielectrics. Electrospinning can also assist in improving the particle distribution in nanocomposite fibers which in response affects greatly the space charge distribution resulting in enhanced dielectric properties.<sup>22</sup> Electrospun PVDF nanofibers have been extensively investigated as piezoelectric nanogenerators or actuators and sensors. However, there are not many studies that implement the composite nanofibers in capacitor applications, <sup>28,29</sup> despite that they bring together the interfacial benefits from electrospinning and the dielectric properties of both materials.

In the present work, nanodielectric systems were developed consisting of a matrix of polydimethylsiloxane (PDMS) reinforced with poly(vinylidene fluoride) (PVDF) electrospun nanofibers and barium titanate (BTO) nanoparticles. The BTO nanoparticles were used to reinforce either the PDMS matrix or the PVDF nanofibers or both and were also subjected to ball milling to reduce their size and break aggregates. The effect of ball milling was additionally investigated toward the dielectric response, relaxation dynamics, and dc charge/discharge capacitor properties. The

morphology of the electrospun nanofibers was identified by means of scanning electron microscopy (SEM), and the dielectric properties were examined in a broad frequency ( $10^{-1}$  to  $10^{5}$  Hz) and temperature (-160 to  $140~^{\circ}$ C) range with broadband dielectric spectroscopy (BDS). Finally, the ability of the nanodielectrics to store and recover capacitive energy was tested in dc conditions by charging and discharging their host capacitors at various voltages ranging from 50 to 300 V and cycle life at a constant voltage (150~V). This work highlights the importance of interfacial area between the constituents of a polymer nanodielectric and how it governs the resulting energy density, efficiency, and dielectric loss values toward improved capacitor performances.

## 2. EXPERIMENTAL SECTION

**2.1. Materials.** A two-part polydimethylsiloxane (PDMS) with  $M_{\rm w} \sim 60000$  g/mol (Dow Corning EI-1184 Optical Encapsulant Kit) was purchased from Ellsworth Adhesives Ltd. and used as the matrix material in the developed polymer nanodielectric systems. According to the manufacturer, this type of PDMS is designed for electronics insulation and thus exhibits stable dielectric properties and high dielectric breakdown strength (19 MV/m) that ensures insulation from large leakage currents. Barium titanate (BTO) particles were purchased from Dow with average diameters ranging from hundreds of nanometers up to a few micrometers. Poly(vinylidene fluoride) (PVDF) with a weight-average molecular weight and a number-average molecular weight of 275 kg/mol and 107 kg/mol, respectively, was obtained from Merck. Dimethylformamide (DMF) and acetone, both purchased from ACROS Organics, were used to dissolve PVDF.

**2.2. Ball Milling of Barium Titanate Particles.** Ball milling was used to reduce the average diameter of BTO, and then ball-milled and pristine particles were separately employed in composite materials and

compared based on the resulting dielectric properties. BTO powder was mixed with DMF, which is one of the components in the solution for dissolving PVDF, and 5 mm alumina balls were used to break aggregates for 13 h by a ball milling machine. The ball-milled BTO/DMF dispersion was directly used for preparation of the PVDF/BTO dispersion intended for electrospinning.

2.3. Electrospinning of PVDF and PVDF/BTO. In this study, PVDF fibers were electrospun with or without BTO particles. Prior to electrospinning, PVDF solutions at a concentration of 22% w/v were prepared by mixing PVDF with DMF and acetone (1.5:1 DMF:acetone ratio) at 60 °C for 3 h until the PVDF pellets were fully dissolved, and the solution became colorless. Subsequently, the BTO particles were added to the PVDF solution at a concentration of 10% w/v (relative to the PVDF solution), and the dispersion was stirred for 1 h. The prepared PVDF solutions and PVDF/BTO dispersion were transferred to 5 mL syringes with steel needles (50 mm length and 0.8 mm diameter), which were later connected to a syringe pump. For the electrospinning process, a positive electrode clip was fixed at the needle, and a negative electrode clip was connected to a metallic plate (collector) covered with aluminum foil. The following experimental parameters were used to produce PVDF fibers and PVDF/BTO fibers: an applied voltage of 11 kV, a flow rate of 0.8 mL/h, and a needle-collector distance of 15 cm.

The positive and negative wires were connected to a direct current—voltage generator to control the voltage between the needle and collector. To optimize the fabrication of the nanosized fibers, four parameters can be controlled: the distance between the needle tip and plate collector, the extrusion speed of pumping machine, the voltage, and the concentration of the solution. The resulting quality of the fibers depends on these four parameters. The fiber quality control was assured by means of optical microscopy until the optimized combination of electrospinning parameters was achieved.

2.4. Preparation of Multilayered Composites. The electrospun mats (PVDF or PVDF/BTO) were cut into pieces of  $3 \times 3$  cm<sup>2</sup>. PDMS prepolymer was prepared by mixing part A solution and part B solution at a ratio of 1:1 with or without BTO particles. Each square of fibrous mat was weighted and placed on a Petri dish. The PDMS prepolymer was poured on the surface of fibers and left for a few minutes to penetrate the mat porosity. If necessary, air bubbles were removed using a needle. Then, another layer of fibers was placed on top of the uncured PDMS, and additional PDMS was poured onto the new layer. This layer-by-layer approach continued until the overall thickness of the composite multilayered structure reached around 1 mm. The composite systems were stored overnight at room temperature to allow for the complete curing of PDMS. The same procedure was used for composites based on PDMS/BTO. In this case, prior to the assembly of the composite systems, PDMS and BTO were mixed in a constant weight ratio of PDMS:BTO equal to 19:1. In Scheme 1, an illustration of the different samples analyzed is provided. In Table 1, a summary of the weight concentrations of the multilayer samples prepared is given. To distinguish between the composite matrix (PDMS/BTO) and the composite fibers (PVDF/ BTO) in Table 1, information about the two phases is provided separately, named Phase A and Phase B, respectively. The characteristic name of each multilayered composite is defined as Phase A + Phase B. The total weight fraction of BTO particles is also provided in the last column of the table as it affects the dielectric properties.

**2.5. Materials Characterization.** The morphology of the materials was investigated by means of scanning electron microscopy (SEM). A Phenom Desktop SEM by ThermoFisher Scientific and a field emission gun scanning electrode microscope (FEG SEM) supplied by JEOL Ltd. were used for this study. Prior to SEM imaging, the samples were coated with Au/Pt. During imaging, a 5 kV accelerated voltage was applied. The morphology of the PVDF/BTO fibers and PDMS+PVDF/BTO fibers is presented in Figures S1 and S2, respectively.

The thermal behavior of the samples was analyzed by means of differential scanning calorimetry (DSC) employing a TA Instruments Q-2000 differential scanning calorimeter. High-precision TZero pans

Table 1. Names and Concentrations of Each Sample Examined in This Study<sup>a</sup>

	phase A (PDMS/BTO) (% w/w)		phase B (PVDF/BTO) (% w/w)		
sample	PDMS	$BaTiO_3$	PVDF	$BaTiO_3$	total BTO (% w/w)
PDMS	100	0	0	0	0
PDMS+PVDF	89.5	0	10.5	0	0
PDMS+PVDF/BTO	92.5	0	6.7	0.8	0.8
PDMS+PVDF/BTO (b-m)	91.5	0	7.6	0.9	0.9
PDMS/BTO	95.0	5.0	0	0	5.0
PDMS/BTO+PVDF	88.9	4.6	6.5	0	4.6
PDMS/BTO+PVDF/ BTO	87.9	4.6	6.7	0.8	5.4
PDMS/BTO+PVDF/ BTO (b-m)	88.8	4.6	5.9	0.7	5.3

"The samples containing ball-milled BTO nanoparticles are designated with "(b-m)" in the first column.

with lids were used, and nitrogen was continuously purged at 50 mL/min during the experiments. A protocol of three consecutive thermal cycles (heating—cooling—heating) from -80 to  $200\,^{\circ}\mathrm{C}$  at a rate of 10  $^{\circ}\mathrm{C/min}$  was used to record the thermal transitions present on the samples under study. The thermal behavior of the samples is presented in Figure S3.

The AC dielectric response of the samples was investigated by means of broadband dielectric spectroscopy (BDS) using a Solatron 1296 dielectric interface in combination with a Schlumberger SI 1260 impedance/phase gain analyzer. The root-mean-square voltage ( $V_{\rm rms}$ ) of the applied field was kept constant at 7 V, while frequency varied from  $10^{-1}$  to  $10^{5}$  Hz. Isothermal scans were conducted in the temperature range from -160 to  $140~{\rm ^{\circ}C}$ , in steps of  $10~{\rm ^{\circ}C}$ . The temperature was controlled via Lake Shore 332 temperature controller, and the gold-coated (KS50X sputter coater; 3 min on each side; 20 mm coated diameter) samples were mounted in a Janis Research STVP-200-XG system cryostat. Liquid nitrogen was employed for cooling at the temperature range of -160 to  $20~{\rm ^{\circ}C}$ , while the entirety of scans was done under a helium atmosphere to avoid condensation and oxidation at low and high temperatures, respectively.

The DC measurements were performed using a 4339B highresistance meter provided by Agilent Technologies (Santa Clara, CA). An automatic measurement process is included in the experimental apparatus to record the charging and discharging electric current. A two parallel-plate electrodes apparatus was used with the sample lying in between throughout the experiment. It should be noted that before every experimental measurement a discharge and short-circuit procedure was performed to avoid the accumulation of charges. To calculate the stored and recovered energy density, the real part of dielectric permittivity was recorded from the dielectric measurements at the lowest measured frequency (0.1 Hz), where the dielectric permittivity is closer to its static value (also referred as dielectric constant) of the material.<sup>30,31</sup> Three types of experiments were conducted for each sample, all at room temperature: (i) Charging Voltage Variation: Six charge and discharge cycles, each at a different voltage from 50 to 300 V with a step of 50 V, were examined. At each time the capacitor was charged for 60 s and discharged, in the absence of applied field, for 360 s. (ii) Capacitor State of Charge: The capacitor was charged at six different voltages, from 50 to 300 V with a step of 50 V at a charging time of 60 s at each level and then gradually discharged, by decreasing the voltage by 50 V each time, for 60 s at each level. (iii) Capacitor Cycle Life: Fifty consecutive charge-discharge cycles at 150 V at constant charging and discharging periods of 30 s.

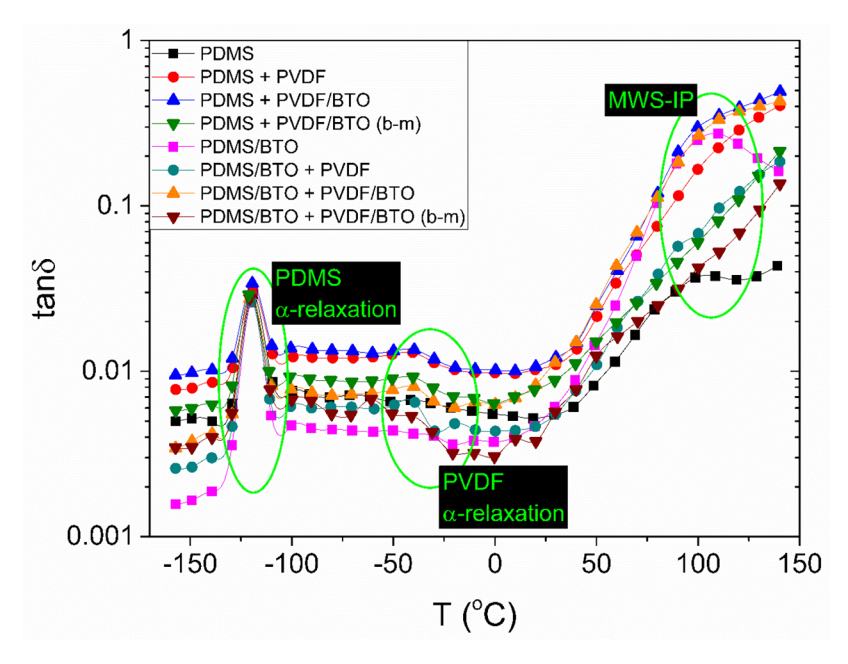


Figure 1. Loss tangent as a function of temperature at 1 Hz for all the systems under study. The dielectric processes observed are highlighted with green circles.

#### 3. RESULTS AND DISCUSSION

**3.1. Dielectric Relaxations.** The dielectric relaxation map of the PDMS-based samples at the examined temperature range is depicted according to broadband dielectric spectroscopy in Figure 1 employing the loss tangent at 1 Hz as a function of temperature. The loss tangent is defined according to eq 1

$$\tan \delta = \frac{\varepsilon''}{\varepsilon'} \tag{1}$$

where  $\varepsilon''$  and  $\varepsilon'$  are the imaginary and real parts of dielectric permittivity, respectively.

Three distinct areas can be seen (highlighted with circles in the graph) with the first being a sharp peak located at -120 °C and attributed to the  $\alpha$ -relaxation of PDMS (known as segmental relaxation or dynamic glass-to-rubber transition process). 32 At about -30 °C a weak peak is visible but only in the case of the samples that contain the PVDF electrospun fibers, and it is attributed to the  $\alpha$ -relaxation of PVDF (dynamic glass-to-rubber transition process).<sup>33</sup> Therefore, this peak should not be associated with the melting of PDMS crystalline fractions because no transition was observed in PVDF-free samples nor any cold crystallization at temperatures between -100 and -80 °C.34 In most cases, the PVDF content is in the range of 6.5% w/w and thus the weakness of the peak. At around 100 °C another peak or shoulder is visible and is attributed to the Maxwell-Wagner-Sillars interfacial polarization (MWS-IP) between the nanocomposites' constituents.<sup>35–38</sup> In addition to interfacial polarization, in the vicinity of 110 °C (Curie temperature), a ferroelectric-toparaelectric structural transition is also expected for barium titanate.<sup>39-41</sup> The aforementioned phase change is easily observable via BDS in BTO microparticles with a characteristic peak in the real part of dielectric permittivity values at low frequencies.<sup>42</sup> In our systems (Figure S5), the ferroelectric-toparaelectric structural transition is clearly observed only in the case of the PDMS + BTO sample ( $T_c = 106$  °C at  $10^{-1}$  Hz). The PVDF-containing samples all exhibit a significant rise of permittivity  $(\varepsilon')$  values at temperatures over 50 °C, ascribed to MWS-IP. Because of its semicrystalline and highly polar nature, even pure PVDF exhibits MWS-IP, between the crystalline and amorphous regions. 43 As a result of the intensity of MWS-IP upon the high-temperature permittivity  $(\varepsilon')$ values, the ferroelectric-to-paraelectric structural transition is not visible for the rest of the materials. The reduction of the BTO particle sizes as a result of ball milling suppresses the phase transition as evident in Figure S5 where no peak is observed via BDS. 42 At the same temperature range, a peak attributed to the MWS-IP is also present at the neat PDMS sample but with considerably lower loss values compared to the other samples. The MWS-IP process for neat PDMS is ascribed to impurities although an additional contribution to high-temperature loss could be attributed to the relaxation of pendant chains. 44,45 Because PDMS is a type B polymer, no normal mode relaxation is expected ascribed to multisegment cooperative chain motions. 46 As it is apparent indirectly in Figure 1 and directly in Figure S5, there are no signs of the parasitic effect of electrode polarization in our samples. The physical mechanism behind electrode polarization is attributed to the immobilization of charge carriers at the interface between the dielectric material and the electrodes and thus the formation of very large dipoles that increase the real and imaginary parts of dielectric permittivity. Because our samples are not electronically semi-conductive nor ionically doped, it is sensible that we do not observe that dielectric phenomenon. In the following sections, each recorded dielectric process is discussed in more detail.

3.1.1. Dynamic Glass-to-Rubber Transition Process of PDMS. The dielectric response of the samples under study at  $-120\,^{\circ}\mathrm{C}$  (the vicinity of glass-to-rubber transition temperature) is provided in a Cole—Cole plot in Figure 2. The addition of the PVDF fibers and the BTO nanoparticles is increasing the dielectric permittivity values, with the highest being the PDMS/BTO sample. Evidently, the samples containing ball-milled BTO nanoparticles exhibited permittivity values comparable with the neat PDMS sample at this

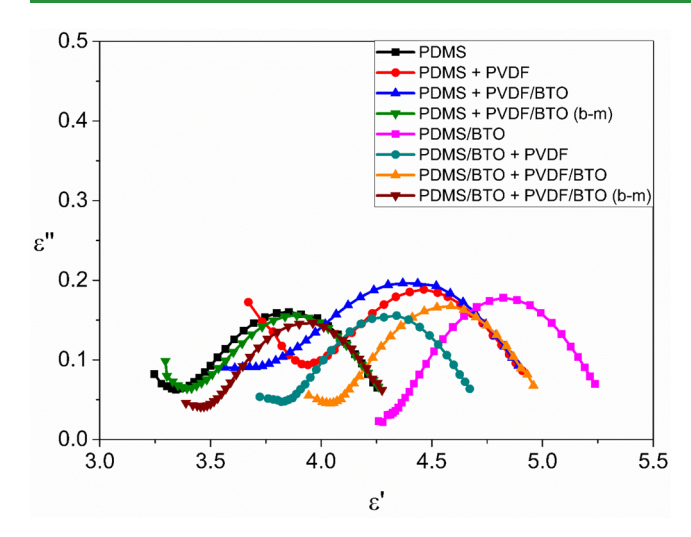


**Figure 2.**  $\alpha$ -Relaxation of PDMS represented in a Cole–Cole plot of all samples under study at -120 °C.

temperature. After ball milling the average size of the BTO nanoparticles decreases, corresponding thus to significant surface area increase that produces stronger polymer—particle adhesion. As a result, the polymer segments responsible for glass-to-rubber transition are less mobile, and thus the orientational polarization is hampered.<sup>47</sup>

3.1.2. Dynamic Glass-to-Rubber Transition Process of PVDF. The glass-to-rubber transition process of the electrospun PVDF fibers, within the PDMS matrix, was observed in the temperature range of -50 to 0 °C (depending on the frequency) which agrees with the literature for bulk PVDF. <sup>48</sup> At  $10^3$  Hz, the  $\alpha$ -relaxation peak is observed at -30 to -20 °C for all the PVDF-containing samples as presented in Figure 3a.

The temperature dependence of the PVDF dynamic glass-to-rubber transition process is presented in Figure 3b where in most cases it follows the Vogel-Fulcher-Tammann-Hesse (VFTH) equation:

$$f = f_0 e^{-DT_V/(T - T_V)}$$
 (2)

where  $f_0$  is a pre-exponential factor that corresponds to the time a molecule needs to move into some free space, and it is expected to follow phonon-like frequency scales, on the order of  $10^{13}$  Hz. $^{49-51}D$  is a dimensionless constant that can be related to the fragility of the relaxation process,  $T_{\rm V}$  the Vogel temperature or ideal glass transition temperature, and T the absolute temperature. Interestingly, the samples containing ball-milled BTO nanoparticles exhibited Arrhenius-type temperature dependence of the  $\alpha$ -relaxation which is attributed to confinement effects.  $^{53,54}$  The Arrhenius equation is

$$f = f_0 e^{-E_A/k_B T} \tag{3}$$

where  $E_{\rm A}$  and  $k_{\rm B}$  are the activation energy and the Boltzmann constant, respectively. In greater detail, the finer size of ball-milled BTO nanoparticles is causing stronger constraints due to the immobility of the ceramic particles; therefore, the cooperative nature of relaxation dynamics diminishes and local fluctuations seems to prevail, as also supported by means of DSC presented in Figure S3b. <sup>52</sup> A similar effect was observed in Figure 2 with the real part of dielectric permittivity values in the vicinity of  $\alpha$ -relaxation of PDMS. The effect that ball-milling has upon the size of BTO nanoparticles was verified and presented in Figure S2 via SEM. The temperature-

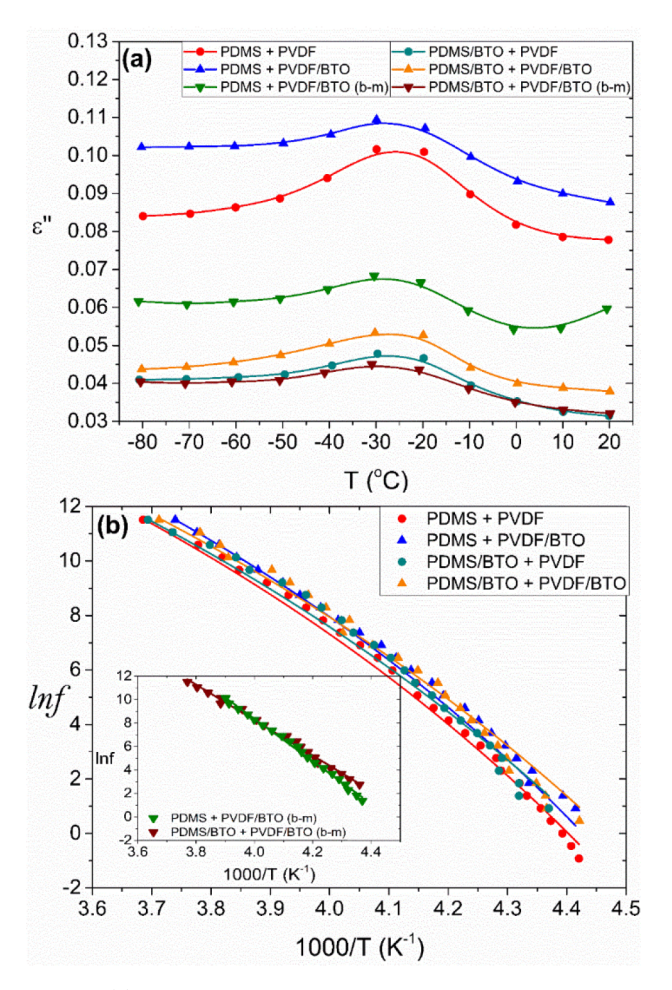


**Figure 3.** (a) Imaginary part of dielectric permittivity as a function of temperature at  $10^3$  Hz to investigate the PVDF α-relaxation process. (b) Temperature and frequency dynamics of the PVDF α-relaxation process which follows a VFTH dependence. As an inset, the relaxation dynamics of the same process in the ball-milled samples is provided which were observed to follow the Arrhenius equation.

dependent dynamics of the PVDF's  $\alpha$ -relaxation are provided in Table S1.

3.1.3. Secondary Relaxations. Figure 4 shows master curves at -120 and -110 °C normalized based on the  $\alpha$ -relaxation intensity and frequency loss peak position. At the low-frequency edge, a weak shoulder is visible only in the case of PVDF-containing samples ascribed to the  $\beta$ -relaxation of PVDF. The molecular mechanism behind the  $\beta$ -relaxation of PVDF is associated with the localized motions of side polar groups in the glassy state and is expected to merge with  $\alpha$ -relaxation at temperatures close and above the glass-to-rubber transition. The fact that the two relaxation processes (the  $\alpha$ -and  $\beta$ -relaxations) are merging at temperatures over the  $T_g$  indicates an association between them. However, the molecular mechanism behind that association is not yet clear, and it is out of the scope of the present work. S4

3.1.4. Maxwell—Wagner—Sillars Interfacial Polarization. Because the contribution of dc conductivity is often masking the high-temperature low-frequency relaxation processes, to discern the interfacial polarization in the dielectric spectra, the complex electric modulus formalism is employed, following eq

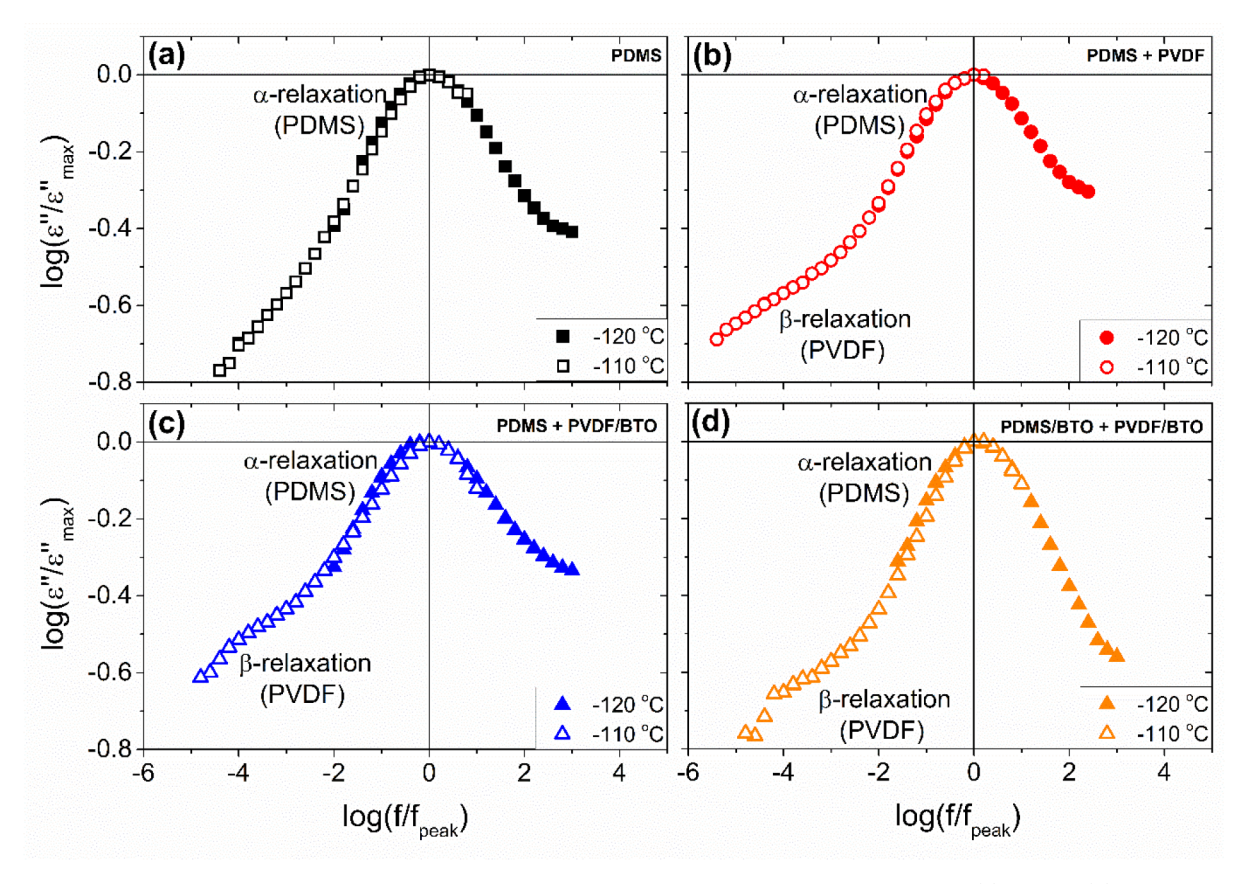


Figure 4. Normalized loss permittivity master curves against normalized frequency at -120 and -110 °C for (a) PDMS, (b) PDMS+PVDF, (c) PDMS+PVDF/BTO, and (d) PDMS/BTO+PVDF/BTO. The loss permittivity and frequency are normalized based on the α-relaxation.

$$M^* = \frac{1}{\varepsilon^*} = \frac{1}{\varepsilon' - i\varepsilon''} = \frac{\varepsilon'}{(\varepsilon')^2 + (\varepsilon'')^2} + i\frac{\varepsilon''}{(\varepsilon')^2 + (\varepsilon'')^2}$$
$$= M' + iM''$$
(4)

where M' and M'' are the real and the imaginary parts of electric modulus, respectively. When the electric modulus formalism is employed, the dc conductivity contribution to the ac dielectric response transforms from a frequency power law to a peak with the value of dc conductivity being directly linked to the frequency loss peak position of the conductivity relaxation. 36,57 It is evident in Figure 5 that at around 75 °C there is a strong peak that is attributed to MWS interfacial polarization between the PDMS matrix and the reinforcements. This effect is visible also in the case of the plain PDMS matrix and is attributed to hardener residuals or catalyst impurities.<sup>58</sup> Apart from MWS-IP, a contribution to the observed high-temperature peak for the BTO-containing samples could be the ferroelectric-to-paraelectric structural transition, particularly on the PDMS+BTO sample. By obtaining the temperature loss peak positions at the examined frequencies, it was possible to examine the frequencytemperature dependence of the MWS-IP for two samples as shown in the insets within Figures 5a and 5b, respectively. In both cases, the dielectric processes followed the Arrhenius model given at eq 3, as expected for interfacial polarization. The comparison between the two samples, PDMS+PVDF/ BTO and PDMS/BTO+PVDF/BTO, shows that the addition of BTO nanoparticles in the PDMS matrix decreases the MWS-IP activation energy, facilitating thus the activation of the interfacial polarization process. At temperatures higher

than 100 °C another process is visible. In the cases where the peak of this process is present within the examined temperature range, a comparison with the loss tangent is made (Figure S4) where the peak is formed when tan  $\delta = 1$ (crossover point between  $\varepsilon'$  and  $\varepsilon''$ ) attributing thus this process to conductivity relaxation. 59,60 From Figure 5 it is also evident that ball milling of the BTO nanoparticles significantly affects the high-temperature dielectric behavior of the examined nanodielectrics; both MWS-IP and conductivity relaxation are pushed to higher temperatures, outside the window of observation of our study. In the case of MWS-IP, higher-temperature loss peak positions are equivalent to longer relaxation times through the time-temperature superposition principle, indicating that greater heterogeneity is caused due to the greater surface area of the ball-milled BTO nanoparticles.<sup>30</sup> The effect that ball milling has on the temperature loss peak position of the conductivity relaxation is discussed later in Figure 5.

As mentioned in Figure 5, the temperature loss peak position of the conductivity relaxation when ball-milled BTO nanoparticles are used is pushed to higher temperatures, which is equivalent to lower frequencies. This result implies a decrease in dc conductivity which is attributed to a greater charge carrier trapping area between the matrix and the reinforcements induced by the increased surface area of the BTO nanoparticles. As it can be appreciated in Figure 6, the presence of ball-milled BTO nanoparticles decreases the ac conductivity at 0.1 Hz by 80% as compared with the corresponding untreated BTO-containing samples. The charge carriers are captured into the traps during their alignment with the applied ac field, decreasing thus the overall electrical

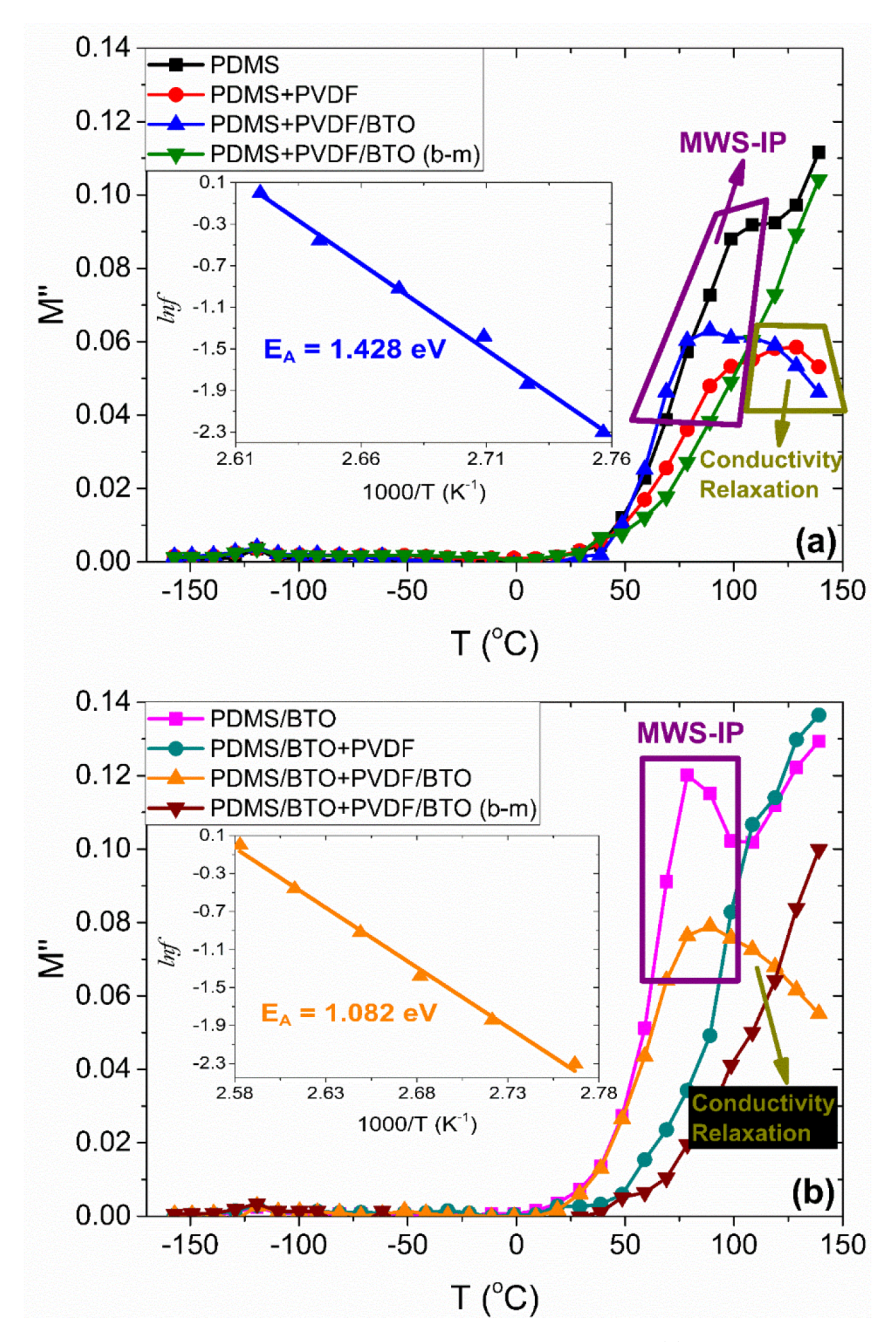


Figure 5. Imaginary part of electric modulus as a function of temperature at 0.1 Hz where at (a) the PDMS-based and (b) PDMS/BTO-based nanodielectrics are presented. The MWS-IP and conductivity relaxations are highlighted, and each subfigure contains an inset with an Arrhenius plot.

conductivity of the material and forming induced dipoles that contribute to the dipolar part of the MWS interfacial polarization. According to Figure S5 and the real part of dielectric permittivity at 0.1 Hz, the high-temperature dielectric process attributed to MWS interfacial polarization appears to have moved at higher temperatures, outside the window of observation, for the ball-milled BTO-containing samples. That agrees with the discussion for Figure 5 when the electric modulus formalism is employed and essentially indicates that the greater interfacial area enhances the impact of heterogeneity which is caused by the ball-milled BTO nanoparticles.<sup>36</sup>

**3.2. Capacitive Energy Storage and Recovery.** One of the many applications requiring polymer-based materials with

enhanced dielectric properties is the development of capacitors with improved capacitive energy storage and efficiency. The stored and recovered energy densities,  $U_s$  and  $U_r$ , respectively, were calculated at 30 °C following eqs 5 and 6

$$U_{s} = \frac{1}{2} \frac{\left(\int I_{c} \, dt\right)^{2}}{\varepsilon' \varepsilon_{0} A^{2}} \tag{5}$$

$$U_r = \frac{1}{2} \frac{\left(\int I_d \, \mathrm{d}t\right)^2}{\varepsilon' \varepsilon_0 A^2} \tag{6}$$

where  $I_c$  and  $I_d$  are the charge and discharge currents, respectively, obtained during the charging and discharging of

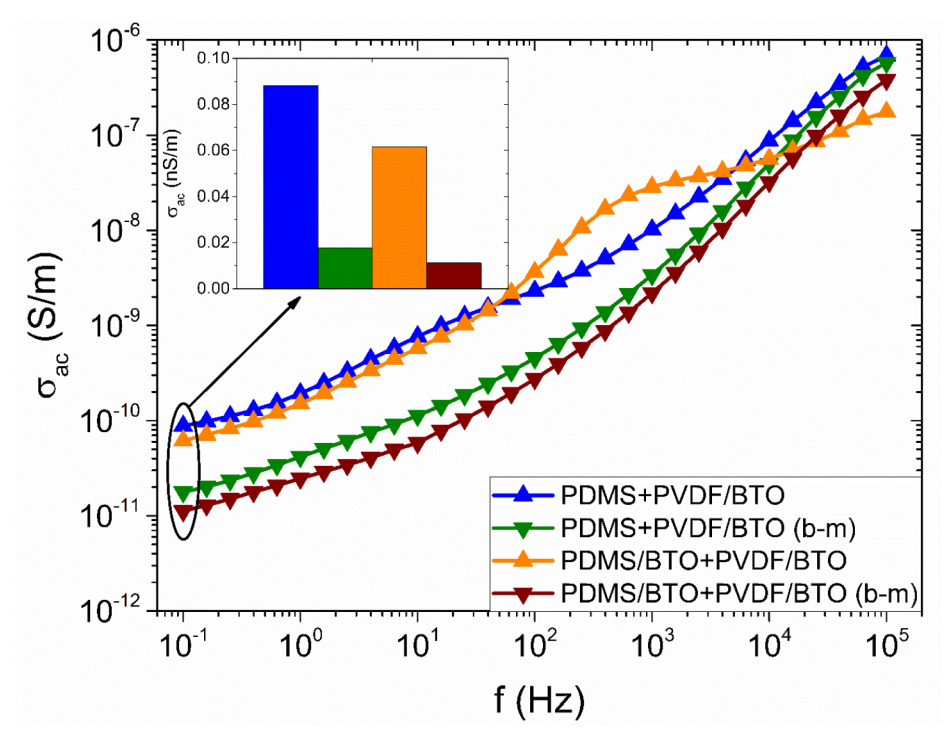


**Figure 6.** The ac conductivity as a function of frequency at 140 °C is provided for the ball-milled BTO their equivalent nontreated BTO nanodielectrics. The inset highlights the ac conductivity values at 0.1 Hz.

the capacitor,  $^{30,61}$   $\varepsilon'$  is the real part of dielectric permittivity measured at 0.1 Hz at 30 °C with broadband dielectric spectroscopy,  $\varepsilon_0$  is the dielectric constant of a vacuum, and A is the effective surface area of the electrodes. To investigate the efficiency of the samples under study, the coefficient of recovery efficiency,  $n_{\rm eff}$  was calculated following eq 7:

$$n_{\text{eff}} = 100\% \frac{U_r}{U_s} \tag{7}$$

Three types of experiments were recorded and are presented below.

3.2.1. Charging Voltage Variation. Figure 7a presents the charge and discharge currents as a function of time for the PDMS/BTO+PVDF/BTO (b-m) sample at charging dc voltages of 50-300 V with a 50 V step. The dc electric field was initially applied to charge the capacitor, and as a result the current intensity decreases exponentially until it reaches a constant value that corresponds to the charge carriers flowing through the interface and can be considered as a kind of leakage current. At 60 s the applied electric field was removed, and as a result the capacitor discharged as indicated by the negative sharp current that gradually reaches a plateau value close to zero. As expected, the charge and discharge currents values increase with increasing voltage. At Figure 7b, the  $U_s$ ,  $U_r$ , and  $n_{\text{eff}}$  are presented for the same sample (PDMS/BTO +PVDF/BTO (b-m)) at 300 V. It is evident that the energy density stored and recovered highly depends on the charging/ discharging time, respectively, with values increasing over 2 orders of magnitude within 60 s. The efficiency of the system appears to be stable, deviating between 75% and 90% with an average value close to 80%. A comparison between all the samples under study at 300 V and 30 s is provided at Figure 7c where the recovered energy density and the coefficient of recovery efficiency are examined. It is evident from the results that the samples containing BTO nanoparticles after ball

milling are the best performing nanocomposites, with the PDMS/BTO+PVDF/BTO (b-m) sample exhibiting 50% improved recovered energy density and 100% improved efficiency than the plain PDMS sample. The improved capacitor performance of the ball-milled BTO containing samples is attributed to the augmented nanoparticle surface. Comparing the performance of the PDMS/BTO+PVDF/BTO (b-m) sample with oriented polyethylene/gold nanocomposites, here we observe double recovered energy density and triple recovery efficiency values, at the same applied voltage.<sup>31</sup> Under the influence of a stronger electric field, we expect that charges that are trapped in the interfaces between the constituents of the nanodielectric materials would be free, by overcoming the potential barriers, and contribute toward the calculation of the stored and recovered energy densities. The result of that would be a greater difference between the performance of nanodielectrics and the plain PDMS. However, this would require different equipment, and it is something that it will to be investigated in a future study.

3.2.2. Capacitor State of Charge. Another test at dc conditions was conducted by gradually increasing the applied electric field to a maximum and then gradually decreasing it—a test that would be closer to real-life operation of a capacitor and at the same time unlock more information about the dielectric material.<sup>62</sup> As it can be seen graphically in Figure 8a, the voltage increases gradually from 50 V up to 300 V in a 50 V step every 60 s, which causes the spikes in the resulting current. The gradual charging of the capacitor is affecting the current spikes in a different way than the distinctive charging/ discharging at different voltages presented previously in Figure 7a. Additionally, the plateau values corresponding to the charge carriers flowing through the interface do indeed increase with increasing voltage, as expected. However, during the gradual discharging period (after 360 s in Figure 8a) the capacitor initially discharges (negative current), but the plateau

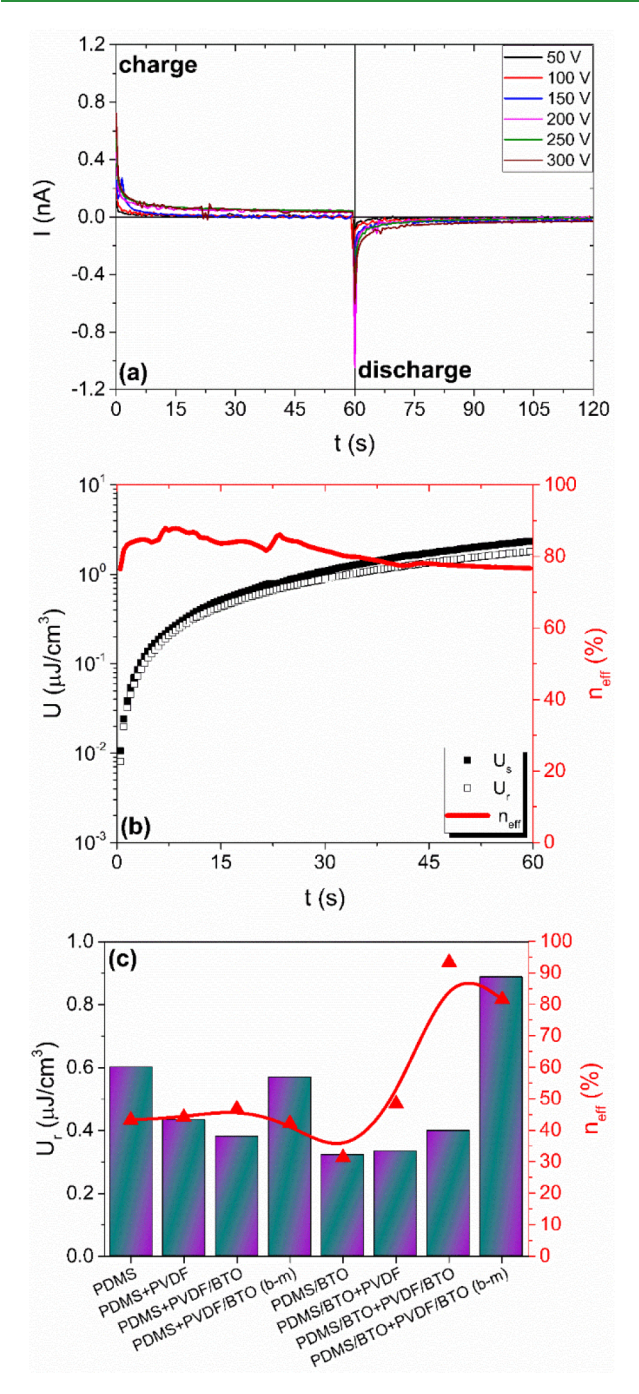
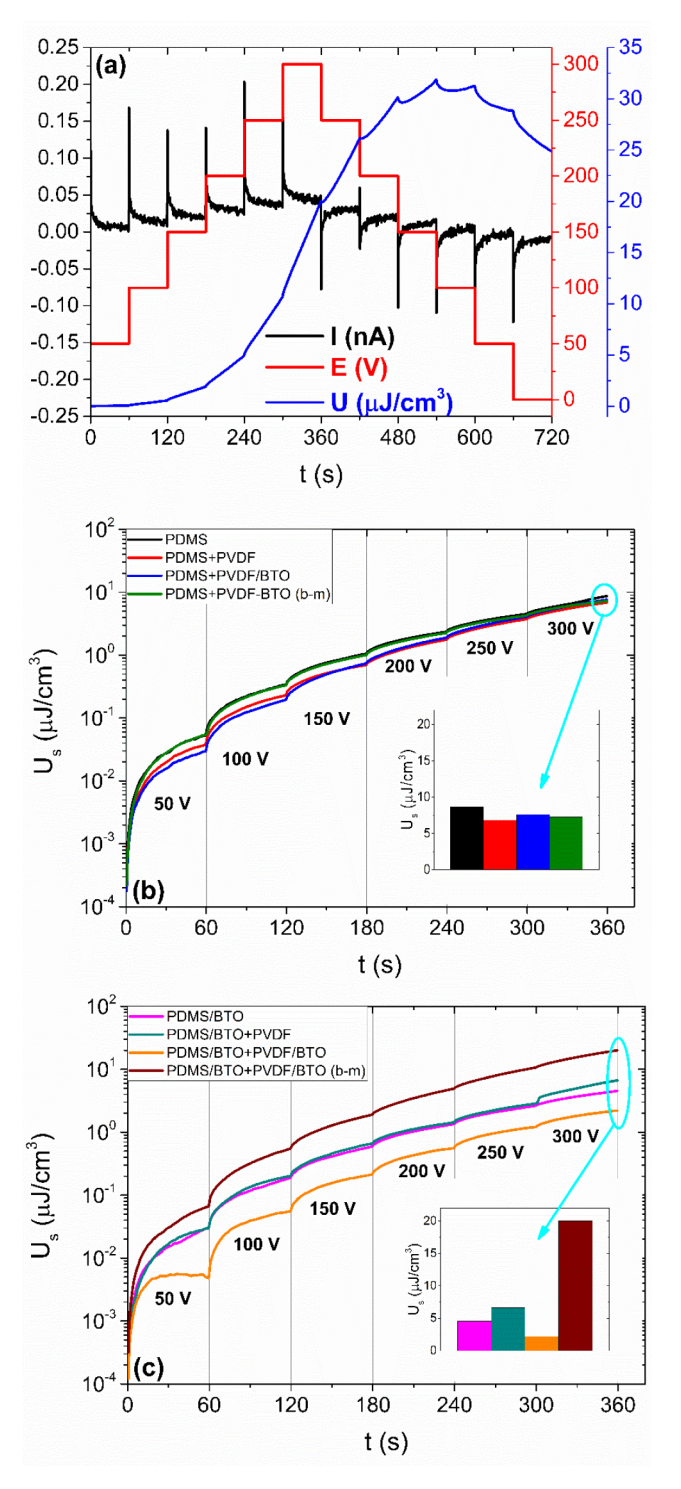


Figure 7. Capacitor behavior at dc conditions for the PDMS/BTO +PVDF/BTO (b-m) sample where (a) the charge and discharge current as a function of time varying the applied charging voltage and (b) the stored and recovered energy densities and coefficient of recovered efficiency at 300 V. (c) Recovered energy density (columns) and coefficient of recovered efficiency (symbols) that corresponds at 30 s and 300 V are provided for all the samples.

values approach and then exceed zero current and as a result the capacitor charges again. This effect can be visually observed in an easier way through the energy density values where the capacitor continuously discharges only after 600 s. This phenomenon is attributed to the fact that the capacitor after the first 360 s is in a partially charged state, and therefore the 50 V decrease step is not enough to completely discharge the capacitor for 60 s. To exclude this effect, in Figures 8b and 8c



**Figure 8.** (a) Applied voltage and resulting current and energy density for the sample PDMS/BTO+PVDF/BTO (b-m). The stored energy density as a function of time for the indicated applied voltages for (b) the PDMS-based and (c) PDMS/BTO-based nanodielectrics. The highest stored energy density values are presented as insets.

we show the data only up to 360 s that correspond to the charging time.

In Figures 8b and 8c the stored energy density values as a function of time for the increased applied dc voltage are presented. According to Figure 8b, it appears that with increasing voltage the nanocomposites' stored energy density is more dependent on the applied voltage than the plain PDMS

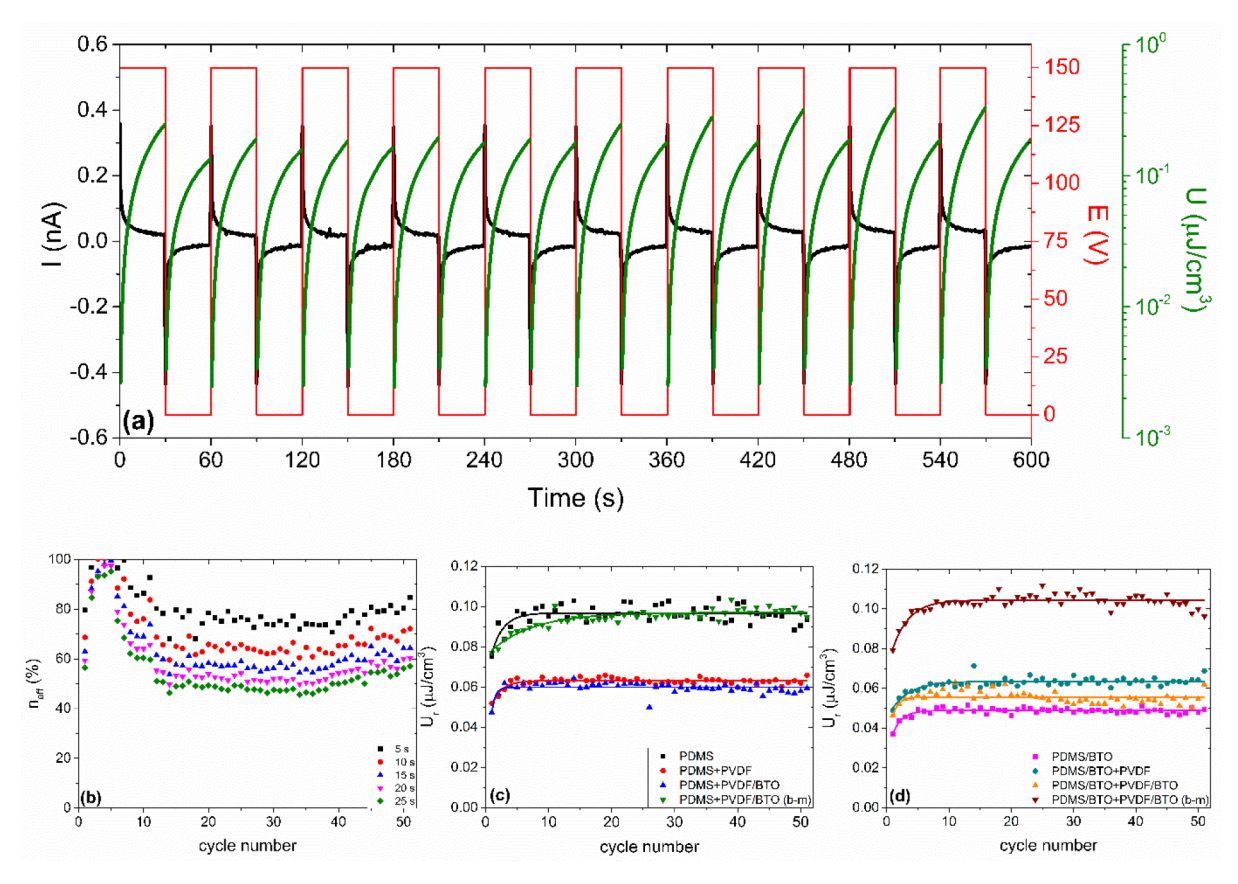


Figure 9. Cycle life behavior of sample PDMS/BTO+PVDF/BTO (b-m): (a) the resulting current and energy density of the first ten charge/discharge cycles and (b) the efficiency as a function of cycle number varying the recorded time. The recovered energy density as a function of cycle life at 15 s for (c) the PDMS-based and (d) PDMS/BTO-based nanodielectrics.

polymer, indicating that at higher voltages they would present improved storage behavior. This finding is attributed to the presence of charge traps, as discussed in Figures 5 and 6, that bound interfacial charges and therefore require a greater applied field to allow the detrapping of the charges. Similar to Figure 7c, the highest values as described by the inset show that the best performing sample is the PDMS/BTO+PVDF/BTO (b-m).

3.2.3. Capacitor Cycle Life. At Figure 9, the cycle life performance of the nanodielectric systems under study is presented at a constant charging voltage of 150 V and discharging at 0 V. Because most capacitors on the market operate at voltages between 50 and 300 V, we chose this voltage value to be in between the average market values. 63 Figure 9a shows the first 10 charge/discharge cycles with the corresponding currents and energy densities of the PDMS/BTO+PVDF/BTO (b-m) sample. For this measurement we charged and discharged the capacitor for 30 s, respectively. According to Figure 9b again for sample PDMS/ BTO+PVDF/BTO (b-m), the efficiency is examined as a function of cycle number, and it exhibits stable values throughout the cycle life of the capacitor after the first five cycles. Within the first five cycles the efficiency is particularly high, even above 100% which is attributed to the insufficient discharge time that leaves residual charges within the capacitor. In addition, it appears to depend strongly on the recorded time, and because the recovered energy density increases over time, a compromise between the two quantities is required and should be optimized for the needs of the application. Here, the efficiency decreases from 80% to 50% after 20 s. For the cycle

life response of all samples, 15 s was chosen as the recorded time, being half of the charge and discharge, respectively, and are presented in Figures 9c and 9d. In all cases, the recorded recovered energy density values initially increase and reach a plateau value after five cycles for most samples. This increase is again attributed to the insufficient discharge time as discussed previously.

All the recovered energy density curves as a function of cycle number, *n*, were fitted with the following exponential function:

$$U_r = U_0 - (\Delta U)e^{-\lambda n} \tag{8}$$

where  $U_0$  is the plateau value,  $\Delta U$  is the difference between the initial value and  $U_0$ , and  $\lambda$  is a reverse time parameter that shows how fast the  $U_r$  values increase against the cycle number. All the parameters' values are provided in Table S2. According to Table S2 and Figure 9d, the sample with the highest  $U_0$ value at 150 V (~0.1 MV/m) is the PDMS/BTO+PVDF/ BTO (b-m), consistently being the better performing nanodielectric system as deduced from all the capacitor charge/ discharge measurements. As opposed to different polymer nanodielectrics at similar low electric fields, the PDMS/BTO +PVDF/BTO (b-m) sample exhibits more than double recovery efficiency against epoxy/BTO and epoxy/SrTiO<sub>3</sub> nanocomposites<sup>56,64</sup> and more than 15 times against unoriented polyethylene/gold nanocomposite.31 The improved behavior of the aforementioned sample is attributed to the improved surface properties of the BTO nanoparticles after ball milling and the resulting augmented interface with the PDMS matrix and the PVDF nanofibers.

#### 4. CONCLUSION

Nanodielectric systems based on polydimethylsiloxane, containing poly(vinylidene fluoride) nanofibers and barium titanate nanoparticles, were fabricated and investigated via differential scanning calorimetry, broadband dielectric spectroscopy, and charge/discharge cycling at dc conditions. High quality bead-free PVDF nanofibers, with or without BTO nanoparticles, were produced by electrospinning and characterized by SEM. Ball-milled BTO nanoparticles were also used to reduce the aggregation effects on the resulting dielectric properties. As a result, improved PVDF/BTO composite nanofibers were produced, indicating the beneficial effect of ball milling. The loss tangent at 1 Hz exhibited three dielectric processes, namely the dynamic glass-to-rubber transition process of PDMS and PVDF nanofibers at -120 and -30 °C, respectively, and an interfacial polarization process close to 100 °C. The dynamic glass-to-rubber transition process of the PVDF nanofibers strongly depends on the size of the BTO nanoparticles because after ball milling there is a shift from VFT to Arrhenius temperature dependence. This change is attributed to confinement effects introduced by the BTO nanoparticles and is supported by SEM and DSC testing. Ball milling of the BTO nanoparticles resulted in the reduction of the dc conductivity due to the greater charge carrier trapping area between the BTO nanoparticles and the polymers involved, as observed at 0.1 Hz employing the  $\sigma_{ac}$  formalism which decreased by 80%. The developed nanodielectrics were examined in a capacitor configuration for energy storage and recovery at dc conditions. Three individual charge/discharge measurements were conducted to test the capacitive ability of the samples at different charging voltages and at gradual charging and discharging and finally to examine their cycle life stability over 50 cycles. According to all the measurements, the best performing sample was the PDMS/BTO+PVDF/BTO with ball-milled BTO nanoparticles that exhibited stable efficiency and recovered energy density of 60% and 0.1  $\mu$ J/ cm<sup>3</sup> at 150 V (~0.1 MV/m) at 15 s charge/discharge time after 50 cycles. This result highlights that the enhanced interfacial properties due to the reduction of the average nanoparticle diameter are paramount to the development of high performing and efficient nanodielectrics.

#### ASSOCIATED CONTENT

## Supporting Information

The Supporting Information is available free of charge at https://pubs.acs.org/doi/10.1021/acsapm.2c01162.

Morphology investigated by SEM, thermal behavior according to DSC, identification of conductivity relaxation via tan  $\delta$  and loss modulus, ferroelectric to paraelectric structural transition of BTO microparticles via BDS (PDF)

## **■** AUTHOR INFORMATION

#### **Corresponding Author**

Stavros X. Drakopoulos — Department of Physics, School of Sciences, University of Bath, Bath BA2 7AY, United Kingdom; The Energy Materials Group, School of Metallurgy and Materials, College of Engineering and Physical Sciences, University of Birmingham, Edgbaston B15 2TT, United Kingdom; ◎ orcid.org/0000-0002-6798-0790; Email: sd2406@bath.ac.uk

#### **Authors**

Jing Yang — Department of Materials, Loughborough University, Leicestershire LE11 3TU, United Kingdom; Department of Chemistry, University of Manchester, Manchester M13 9PL, United Kingdom

Orestis Vryonis — Tony Davies High Voltage Laboratory, Department of Electronic and Computer Science, Faculty of Engineering and Physical Sciences, University of Southampton, Southampton SO17 1BJ, United Kingdom; Orcid.org/0000-0002-2862-4494

Leah Williams – Department of Materials, Loughborough University, Leicestershire LE11 3TU, United Kingdom Georgios C. Psarras – Smart Materials & Nanodielectrics

Laboratory, Department of Materials Science, University of Patras, Patras 26504, Hellas (Greece); orcid.org/0000-0002-0539-2838

Elisa Mele — Department of Materials, Loughborough University, Leicestershire LE11 3TU, United Kingdom; orcid.org/0000-0003-3574-7684

Complete contact information is available at: https://pubs.acs.org/10.1021/acsapm.2c01162

#### **Author Contributions**

S.X.D.: conceptualization, methodology, investigation, formal analysis, visualization, software, writing-original draft, writing-review and editing; J.Y.: methodology, investigation, writing-review and editing; (O.V.) methodology, investigation, resources, writing-review and editing; L.W.: investigation; G.C.P.: project administration, resources, writing-review and editing; E.M.: conceptualization, methodology, project administration, resources, writing-review and editing, funding acquisition.

#### **Notes**

The authors declare no competing financial interest.

#### ACKNOWLEDGMENTS

The authors acknowledge the use of the facilities in the Loughborough Materials Characterization Centre, Department of Materials, for SEM analysis. The authors also thank Dr Hongtao Zhang from Loughborough University for providing the ball milling machine.

#### REFERENCES

- (1) Newell, P. Trasformismo or Transformation? The Global Political Economy of Energy Transitions. *Rev. Int. Polit. Econ.* **2019**, 26 (1), 25–48.
- (2) Schmidt, O.; Hawkes, A.; Gambhir, A.; Staffell, I. The Future Cost of Electrical Energy Storage Based on Experience Rates. *Nat. Energy* **2017**, *2* (8), 17110.
- (3) Krauss, L. M.Physics of Climate Change; Post Hill Press: 2021.
- (4) Schadler, L. S.; Nelson, J. K. Polymer Nanodielectrics—Short History and Future Perspective. *J. Appl. Phys.* **2020**, 128 (12), 120902.
- (5) Xie, Y.; Wang, J.; Tan, S.; Peng, B.; Qiao, B.; Zhang, Z.; Huang, X.; Sui, H. Improving Energy Storage Density and Efficiency of Polymer Dielectrics by Adding Trace Biomimetic Lysozyme-Modified Boron Nitride. ACS Appl. Energy Mater. 2020, 3 (8), 7952–7963.
- (6) Yao, Z.; Song, Z.; Hao, H.; Yu, Z.; Cao, M.; Zhang, S.; Lanagan, M. T.; Liu, H. Homogeneous/Inhomogeneous-Structured Dielectrics and Their Energy-Storage Performances. *Adv. Mater.* **2017**, *29* (20), 1601727.
- (7) Zhang, X.; Shen, Y.; Xu, B.; Zhang, Q.; Gu, L.; Jiang, J.; Ma, J.; Lin, Y.; Nan, C.-W. Giant Energy Density and Improved Discharge Efficiency of Solution-Processed Polymer Nanocomposites for Dielectric Energy Storage. *Adv. Mater.* **2016**, 28 (10), 2055–2061.

- (8) Lau, K. Y.; Vaughan, A. S.; Chen, G. Nanodielectrics: Opportunities and Challenges. *IEEE Electr. Insul. Mag.* **2015**, *31* (4), 45–54.
- (9) Li, B.; Salcedo-Galan, F.; Xidas, P. I.; Manias, E. Improving Electrical Breakdown Strength of Polymer Nanocomposites by Tailoring Hybrid-Filler Structure for High-Voltage Dielectric Applications. ACS Appl. Nano Mater. 2018, 1 (9), 4401–4407.
- (10) Li, B.; Manias, E. Increased Dielectric Breakdown Strength of Polyolefin Nanocomposites via Nanofiller Alignment. *MRS Adv.* **2017**, 2 (6), 357–362.
- (11) Lau, K.; Vaughan, A.; Chen, G.; Hosier, I.; Holt, A.; Ching, K. On the Space Charge and DC Breakdown Behavior of Polyethylene/Silica Nanocomposites. *IEEE Trans. Dielectr. Electr. Insul.* **2014**, 21 (1), 340–351.
- (12) Tan, D. Q. Review of Polymer-Based Nanodielectric Exploration and Film Scale-Up for Advanced Capacitors. *Adv. Funct. Mater.* **2020**, *30* (18), 1808567.
- (13) Niu, Y.; Yu, K.; Bai, Y.; Wang, H. Enhanced Dielectric Performance of BaTiO<sub>3</sub>/PVDF Composites Prepared by Modified Process for Energy Storage Applications. *IEEE Trans. Ultrason. Ferroelectr. Freq. Control* **2015**, 62 (1), 108–115.
- (14) Hao, Y. N.; Wang, X. H.; O'Brien, S.; Lombardi, J.; Li, L. T. Flexible BaTiO <sub>3</sub> /PVDF Gradated Multilayer Nanocomposite Film with Enhanced Dielectric Strength and High Energy Density. *J. Mater. Chem. C* **2015**, 3 (37), 9740–9747.
- (15) Dang, Z.-M.; Yuan, J.-K.; Yao, S.-H.; Liao, R.-J. Flexible Nanodielectric Materials with High Permittivity for Power Energy Storage. *Adv. Mater.* **2013**, *25* (44), 6334–6365.
- (16) Roy, M.; Nelson, J. K.; MacCrone, R. K.; Schadler, L. S.; Reed, C. W.; Keefe, R.; Zenger, W. Polymer Nanocomposite Dielectrics the Role of the Interface. *IEEE Trans. Dielectr. Electr. Insul.* **2005**, *12* (4), 629–643.
- (17) Liu, G.; Zhang, T.; Feng, Y.; Zhang, Y.; Zhang, C.; Zhang, Y.; Wang, X.; Chi, Q.; Chen, Q.; Lei, Q. Sandwich-Structured Polymers with Electrospun Boron Nitrides Layers as High-Temperature Energy Storage Dielectrics. *Chem. Eng. J.* **2020**, 389, 124443.
- (18) Bhattacharya, S.; Roy, I.; Tice, A.; Chapman, C.; Udangawa, R.; Chakrapani, V.; Plawsky, J. L.; Linhardt, R. J. High-Conductivity and High-Capacitance Electrospun Fibers for Supercapacitor Applications. *ACS Appl. Mater. Interfaces* **2020**, *12* (17), 19369–19376.
- (19) Wu, Y.-H.; Zha, J.-W.; Yao, Z.-Q.; Sun, F.; Li, R. K. Y.; Dang, Z.-M. Thermally Stable Polyimide Nanocomposite Films from Electrospun BaTiO <sub>3</sub> Fibers for High-Density Energy Storage Capacitors. *RSC Adv.* **2015**, *5* (56), 44749–44755.
- (20) Subbiah, T.; Bhat, G. S.; Tock, R. W.; Parameswaran, S.; Ramkumar, S. S. Electrospinning of Nanofibers. *J. Appl. Polym. Sci.* **2005**, *96* (2), 557–569.
- (21) Li, X.; Chen, W.; Qian, Q.; Huang, H.; Chen, Y.; Wang, Z.; Chen, Q.; Yang, J.; Li, J.; Mai, Y. Electrospinning-Based Strategies for Battery Materials. *Adv. Energy Mater.* **2021**, *11* (2), 2000845.
- (22) Hu, J.; Zhang, S.; Tang, B. Rational Design of Nanomaterials for High Energy Density Dielectric Capacitors via Electrospinning. *Energy Storage Mater.* **2021**, *37*, 530–555.
- (23) Katsouras, I.; Asadi, K.; Li, M.; van Driel, T. B.; Kjær, K. S.; Zhao, D.; Lenz, T.; Gu, Y.; Blom, P. W. M.; Damjanovic, D.; Nielsen, M. M.; de Leeuw, D. M. The Negative Piezoelectric Effect of the Ferroelectric Polymer Poly(Vinylidene Fluoride). *Nat. Mater.* **2016**, *15* (1), 78–84.
- (24) Lee, C.; Wood, D.; Edmondson, D.; Yao, D.; Erickson, A. E.; Tsao, C. T.; Revia, R. A.; Kim, H.; Zhang, M. Electrospun Uniaxially-Aligned Composite Nanofibers as Highly-Efficient Piezoelectric Material. *Ceram. Int.* **2016**, 42 (2), 2734–2740.
- (25) Zhao, Y.; Yin, L.; Zhong, S.; Zha, J.; Dang, Z. Review of Dielectric Elastomers for Actuators, Generators and Sensors. *IET Nanodielectrics* **2020**, 3 (4), 99–106.
- (26) Abolhasani, M. M.; Naebe, M.; Shirvanimoghaddam, K.; Fashandi, H.; Khayyam, H.; Joordens, M.; Pipertzis, A.; Anwar, S.; Berger, R.; Floudas, G.; Michels, J.; Asadi, K. Thermodynamic

- Approach to Tailor Porosity in Piezoelectric Polymer Fibers for Application in Nanogenerators. *Nano Energy* **2019**, *62*, 594–600.
- (27) Abolhasani, M. M.; Azimi, S.; Mousavi, M.; Anwar, S.; Hassanpour Amiri, M.; Shirvanimoghaddam, K.; Naebe, M.; Michels, J.; Asadi, K. Porous Graphene/Poly(Vinylidene Fluoride) Nanofibers for Pressure Sensing. J. Appl. Polym. Sci. 2022, 139 (14), 51907.
- (28) Wang, Y.; Yao, M.; Ma, R.; Yuan, Q.; Yang, D.; Cui, B.; Ma, C.; Liu, M.; Hu, D. Design Strategy of Barium Titanate/Polyvinylidene Fluoride-Based Nanocomposite Films for High Energy Storage. *J. Mater. Chem. A* **2020**, *8* (3), 884–917.
- (29) Liu, S.; Xue, S.; Zhang, W.; Zhai, J. Enhanced Dielectric and Energy Storage Density Induced by Surface-Modified BaTiO3 Nanofibers in Poly(Vinylidene Fluoride) Nanocomposites. *Ceram. Int.* **2014**, *40* (10), 15633–15640.
- (30) Manika, G. C.; Psarras, G. C. Energy Storage and Harvesting in BaTiO <sub>3</sub> /Epoxy Nanodielectrics. *High Volt.* **2016**, *1* (4), 151–157.
- (31) Drakopoulos, S. X.; Manika, G. C.; Nogales, A.; Kim, T.; Robbins, A. B.; Claudio, G.; Minnich, A. J.; Ezquerra, T. A.; Psarras, G. C.; Martin-Fabiani, I.; Ronca, S. Gold/Ultra-high Molecular Weight Polyethylene Nanocomposites for Electrical Energy Storage: Enhanced Recovery Efficiency upon Uniaxial Deformation. *J. Appl. Polym. Sci.* 2021, 138 (42), 51232.
- (32) Klonos, P.; Panagopoulou, A.; Kyritsis, A.; Bokobza, L.; Pissis, P. Dielectric Studies of Segmental Dynamics in Poly-(Dimethylsiloxane)/Titania Nanocomposites. *J. Non-Cryst. Solids* **2011**, 357 (2), 610–614.
- (33) Grimau, M.; Laredo, E.; Bello, A.; Suarez, N. Correlation between Dipolar TSDC and AC Dielectric Spectroscopy at the PVDF Glass Transition. *J. Polym. Sci., Part B: Polym. Phys.* **1997**, 35 (15), 2483–2493.
- (34) Klonos, P. A. Crystallization, Glass Transition, and Molecular Dynamics in PDMS of Low Molecular Weights: A Calorimetric and Dielectric Study. *Polymer* **2018**, *159*, 169–180.
- (35) Broadband Dielectric Spectroscopy; Kremer, F., Schönhals, A., Eds.; Springer: Berlin, 2003.
- (36) Tsangaris, G. M.; Psarras, G. C.; Kouloumbi, N. Electric Modulus and Interfacial Polarization in Composite Polymeric Systems. J. Mater. Sci. 1998, 33 (8), 2027–2037.
- (37) Feng, Y.; Li, W. L.; Hou, Y. F.; Yu, Y.; Cao, W. P.; Zhang, T. D.; Fei, W. D. Enhanced Dielectric Properties of PVDF-HFP/BaTiO <sup>3</sup> -Nanowire Composites Induced by Interfacial Polarization and Wire-Shape. *I. Mater. Chem. C* **2015**, 3 (6), 1250–1260.
- (38) Sun, L.; Shi, Z.; Liang, L.; Wei, S.; Wang, H.; Dastan, D.; Sun, K.; Fan, R. Layer-Structured BaTiO <sub>3</sub> /P(VDF-HFP) Composites with Concurrently Improved Dielectric Permittivity and Breakdown Strength toward Capacitive Energy-Storage Applications. *J. Mater. Chem. C* 2020, 8 (30), 10257–10265.
- (39) Forsbergh, P. W. Domain Structures and Phase Transitions in Barium Titanate. *Phys. Rev.* **1949**, *76* (8), 1187–1201.
- (40) Slater, J. C. The Lorentz Correction in Barium Titanate. *Phys. Rev.* **1950**, 78 (6), 748–761.
- (41) Zhang, T.; Zhao, X.; Zhang, C.; Zhang, Y.; Zhang, Y.; Feng, Y.; Chi, Q.; Chen, Q. Polymer Nanocomposites with Excellent Energy Storage Performances by Utilizing the Dielectric Properties of Inorganic Fillers. *Chem. Eng. J.* **2021**, *408*, 127314.
- (42) Manika, G. C.; Andrikopoulos, K. S.; Psarras, G. C. On the Ferroelectric to Paraelectric Structural Transition of BaTiO3Micro-/Nanoparticles and Their Epoxy Nanocomposites. *Molecules* **2020**, 25 (11), 2686.
- (43) Rekik, H.; Ghallabi, Z.; Royaud, I.; Arous, M.; Seytre, G.; Boiteux, G.; Kallel, A. Dielectric Relaxation Behaviour in Semi-Crystalline Polyvinylidene Fluoride (PVDF)/TiO<sub>2</sub> Nanocomposites. *Compos. Part B Eng.* **2013**, 45 (1), 1199–1206.
- (44) Villar, M. A.; Vallés, E. M. Influence of Pendant Chains on Mechanical Properties of Model Poly(Dimethylsiloxane) Networks. 2. Viscoelastic Properties. *Macromolecules* **1996**, 29 (11), 4081–4089.
- (45) Villar, M. A.; Bibbó, M. A.; Vallés, E. M. Influence of Pendant Chains on Mechanical Properties of Model Poly(Dimethylsiloxane)

- Networks. 1. Analysis of the Molecular Structure of the Network. *Macromolecules* **1996**, 29 (11), 4072–4080.
- (46) Lorthioir, C.; Alegría, A.; Colmenero, J.; Deloche, B. Heterogeneity of the Segmental Dynamics of Poly(Dimethylsiloxane) in a Diblock Lamellar Mesophase: Dielectric Relaxation Investigations. *Macromolecules* **2004**, *37* (20), 7808–7817.
- (47) Vryonis, O.; Anastassopoulos, D. L.; Vradis, A. A.; Psarras, G. C. Dielectric Response and Molecular Dynamics in Epoxy-BaSrTiO3 Nanocomposites: Effect of Nanofiller Loading. *Polymer* **2016**, *95*, 82–90.
- (48) Linares, A.; Nogales, A.; Rueda, D. R.; Ezquerra, T. A. Molecular Dynamics in PVDF/PVA Blends as Revealed by Dielectric Loss Spectroscopy. *J. Polym. Sci., Part B: Polym. Phys.* **2007**, 45 (13), 1653–1661.
- (49) Cohen, M. H.; Turnbull, D. Molecular Transport in Liquids and Glasses. *J. Chem. Phys.* **1959**, *31* (5), 1164–1169.
- (50) Cohen, M. H.; Grest, G. S. Dispersion of Relaxation Rates in Dense Liquids and Glasses. *Phys. Rev. B* 1981, 24 (7), 4091–4094.
- (51) Angell, C. A. Why C1 = 16–17 in the WLF Equation Is Physical—and the Fragility of Polymers. *Polymer* **1997**, 38 (26), 6261–6266.
- (52) Martinez-Garcia, J. C.; Rzoska, S. J.; Drozd-Rzoska, A.; Starzonek, S.; Mauro, J. C. Fragility and Basic Process Energies in Vitrifying Systems. *Sci. Rep.* **2015**, *5* (1), 8314.
- (53) Schönhals, A.; Goering, H.; Schick, C.; Frick, B.; Mayorova, M.; Zorn, R. Segmental Dynamics of Poly(Methyl Phenyl Siloxane) Confined to Nanoporous Glasses. *Eur. Phys. J. Spec. Top.* **2007**, *141* (1), 255–259.
- (54) Kremer, F.; Huwe, A.; Schönhals, A.; Różański, S. A.Molecular Dynamics in Confining Space. In *Broadband Dielectric Spectroscopy*; Kremer, F., Schönhals, A., Eds.; Springer: Berlin, 2003; pp 171–224.
- (55) Linares, A.; Nogales, A.; Rueda, D. R.; Ezquerra, T. A. Molecular Dynamics in PVDF/PVA Blends as Revealed by Dielectric Loss Spectroscopy. *J. Polym. Sci., Part B: Polym. Phys.* **2007**, 45 (13), 1653–1661.
- (56) Sy, J. W.; Mijovic, J. Reorientational Dynamics of Poly-(Vinylidene Fluoride)/Poly(Methyl Methacrylate) Blends by Broad-Band Dielectric Relaxation Spectroscopy. *Macromolecules* **2000**, 33 (3), 933–946.
- (57) Hodge, I. M.; Ngai, K. L.; Moynihan, C. T. Comments on the Electric Modulus Function. *J. Non-Cryst. Solids* **2005**, 351 (2), 104–115.
- (58) Iannarelli, A.; Ghaffarian Niasar, M.; Ross, R. Electrode Interface Polarization Formation in Dielectric Elastomer Actuators. Sens. Actuators Phys. 2020, 312, 111992.
- (59) Drakopoulos, S. X.; Patsidis, A. C.; Psarras, G. C. Epoxy-Based/BaTiO3 Nanodielectrics: Relaxation Dynamics, Charge Transport and Energy Storage. *Mater. Res. Bull.* **2022**, *145*, 111537.
- (60) Richert, R.; Agapov, A.; Sokolov, A. P. Appearance of a Debye Process at the Conductivity Relaxation Frequency of a Viscous Liquid. *J. Chem. Phys.* **2011**, *134* (10), 104508.
- (61) Manika, G. C.; Psarras, G. C. Barium Titanate/Epoxy Resin Composite Nanodielectrics as Compact Capacitive Energy Storing Systems. *Express Polym. Lett.* **2019**, *13* (8), 749–758.
- (62) Khazraei, M.; Sepahvand, H.; Corzine, K. A.; Ferdowsi, M. Active Capacitor Voltage Balancing in Single-Phase Flying-Capacitor Multilevel Power Converters. *IEEE Trans. Ind. Electron.* **2012**, 59 (2), 769–778.
- (63) Yializis, A.Polymeric Monolithic Capacitor. US 2020/0194179 A1, June 18, 2020.
- (64) Manika, G. C.; Psarras, G. C. SrTiO <sub>3</sub> /Epoxy Nanodielectrics as Bulk Energy Storage and Harvesting Systems: The Role of Conductivity. *ACS Appl. Energy Mater.* **2020**, *3* (1), 831–842.

## **□** Recommended by ACS

Polyurethane-Coated Polyaniline/SiO<sub>2</sub> Nanoparticle Electrospun Nanofiber Membranes for Waterproof and Moisture-Permeable Materials

Yuqing Yi, Ni Li, et al. NOVEMBER 03, 2022

ACS APPLIED NANO MATERIALS

READ 🗹

## Dielectric Properties and Flexibility of Polyacrylonitrile/Graphene Oxide Composite Nanofibers

Muhammad Rama Almafie, Ida Sriyanti, et al.

SEPTEMBER 07, 2022

ACS OMEGA

READ 🗹

## Crystallization, Phase Stability, Microstructure, and Chemical Bonding in Ga<sub>2</sub>O<sub>3</sub> Nanofibers Made by Electrospinning

Nanthakishore Makeswaran, C. V. Ramana, et al.

SEPTEMBER 01, 2022

ACS OMEGA

READ **C** 

## Nanostructural Engineering of Electrospun Poly(vinyl alcohol)/Carbon Nanotube Mats into Dense Films for Alcohol Dehydration

Su Kyung Kang, Soo-Hwan Jeong,  $\it et~\it al.$ 

SEPTEMBER 29, 2022

ACS SUSTAINABLE CHEMISTRY & ENGINEERING

READ 🗹

Get More Suggestions >